Dual Synchronous Rotating Frame Current Control of Brushless Doubly Fed Induction Generator Under Unbalanced Network

Litong Xu, *Student Member, IEEE*, Ming Cheng, *Fellow, IEEE*, Xinchi Wei, *Member, IEEE*, Xiaoming Yan, *Student Member, IEEE*, and Yu Zeng, *Student Member, IEEE*

***Abstract*—This article investigates the modeling and control of brushless doubly fed induction generator (BDFIG) under an unbalanced network. The system behavior of BDFIG under the unbalanced grid voltage is analyzed. The control strategies and different control targets of BDFIG in balanced and unbalanced networks are discussed. In order to achieve control targets, a current control strategy consisting of a primary controller and a secondary controller for the control winding is proposed. The primary controller is implemented in the positive-sequence synchronous rotating frame (SRF) to ensure the dynamic response of the system without sequence components separation, whereas the secondary controller is implemented in the negative-sequence SRF to control the negative-sequence current component only. A feedforward compensation for the negative-sequence current control is used to mitigate the sequence components separation influence on the dynamic response of the secondary controller. Experimental results demonstrate the effectiveness of the control strategy in suppressing the power and current oscillation of a BDFIG system under the unbalanced network.**

***Index Terms*—Brushless doubly fed induction generator (BDFIG), feedforward compensation, primary controller, secondary controller, unbalanced network.**

NOMENCLATURE

A. Main Variables

f	Current frequency (Hz).
F	Electromagnetic quantities.
g	Controller gain.
$\boldsymbol{i}$	Instantaneous current (A).
k	Coefficient [$k = L_{mp}L_{mc}/(L_{ps}L_r{}')$].
k_1	Coefficient ($k_1 = L_r/L_r{}'$).
k_2	Coefficient ($k_2 = L_{mc}/L_{mp}$).
k_p and k_i	Proportional and integral gain.
L	Inductance (H).
$L_r{}'$	Rotor transient inductance ($L_r{}' = L_r$–$L_{mp}{}^2/L_{ps}$).
n	Shaft speed (r/min).
p	Number of pole pairs.
R	Resistance (Ω).
T_r	Rotor time constant ($T_r = L_r/R_r$).
$T_r{}'$	Rotor transient time constant ($T_r{}' = L_r{}'/R_r$).
$\boldsymbol{u}$	Instantaneous voltage (V).
$\boldsymbol{\psi}$	Flux linkage (Wb).
ω	Electrical angular velocity (rad/s).
$\boldsymbol{\Omega}_m$	Mechanical angular velocity (rad/s).

B. Subscript and Superscript Variables

$\alpha\beta$	Stationary coordinate system.
dq	Rotating coordinate system.
m	Magnetizing.
N	Synchronous mode.
p, r, and c	Power, rotor, and control winding.
s	Stator.
t	Time.
σ	Leakage.

Manuscript received June 16, 2020; revised September 19, 2020; accepted November 11, 2020. Date of publication November 23, 2020; date of current version February 5, 2021. This work was supported by the National Natural Science Foundation of China under Project 61973073. Recommended for publication by Associate Editor A. K. Gupta. *(Corresponding author: Ming Cheng.)*

Litong Xu, Ming Cheng, Xiaoming Yan, and Yu Zeng are with the School of Electrical Engineering, Southeast University, Nanjing 210096, China (e-mail: xulitong_ee@163.com; mcheng@seu.edu.cn; 13604074464@163.com; zengyu92@foxmail.com).

Xinchi Wei is with the State Grid Shanghai Electric Power Research Institute, Shanghai 200437, China (e-mail: newlate@126.com).

Color versions of one or more figures in this article are available at https://doi.org/10.1109/TPEL.2020.3039537.

Digital Object Identifier 10.1109/TPEL.2020.3039537

I. INTRODUCTION

OVER the past few decades, the development and utilization of wind energy has received increasing attention due to the dramatic increase in fossil fuel consumption and environmental pollution [1]. According to the GWEC report [2], more than 60 GW of wind energy capacity was newly installed all over the world, and the cumulative installed capacity has reached 650 GW in 2019. With the development of large wind turbine systems, the penetration of wind power to the grid is increasing. Considering the increasingly high grid standards, a number of issues have gained attention, including mitigating the adverse effects of wind power systems on the grid under severe grid condition and improving low-voltage ride-through capability [3].

The doubly fed induction generator (DFIG) [4]–[7] is the most widely used in wind power generation because the generation system requires only a partially rated converter and two electrical ports can achieve more flexible control. However, the existence of brushes and slip rings results in high operation losses, frequent maintenance, and overhaul under harsh conditions; therefore,

DFIG has low reliability and high maintenance costs. The brushless doubly fed generator (BDFG) is considered an alternative to DFIG due to its high reliability and low-cost benefits and it shows great potential in variable speed wind turbines [1], [4], [8], [9]. The BDFG system converter requires only a partial power rating. The elimination of brushes and slip rings significantly improves reliability and reduces maintenance costs while retaining all the benefits of DFIG.

There are four main topological structures of BDFG: cascaded brushless doubly fed induction generator (BDFIG); nested ring rotor BDFIG; brushless doubly fed reluctance machine (BDFRM); and dual-stator BDFIG. These machines have common features: two sets of stator winding, one mechanical port, and no slip rings or brushes. Cascaded BDFIG consists of two wound rotor induction machines with a common shaft. Two sets of rotor winding are connected in the same or reverse-phase sequence [10]. Two stator magnetic fields are mutually independent without coupling directly. However, the axial length is too long to be applied in a limited space. The nested ring rotor BDFIG contains two sets of stator winding on the same stator core and a nested ring rotor [11], [12]. The BDFRM contains two sets of stator winding with different pole pairs on the same stator core and a reluctance rotor [13], [14]. These two machines differ in the rotor structure but they both have a stator core and a rotor for their working principle of the magnetic field modulation [15]. Although the nested ring rotor BDFIG and BDFRM are compact in structure, a large number of spatial harmonics cause extra torque oscillation and acoustic noise. Dual-stator BDFIG consists of three parts: an external stator with power winding (PW), an internal stator with control winding (CW), and a nonmagnetic support rotor with the double-layer iron cores [16], [17]. Two sets of rotor winding are connected in the same or reverse-phase sequence and placed on two layers of iron cores, respectively. Dual-stator BDFIG can make full use of the machine internal space to increase the power density. As for other types of induction generators with dual-stator winding, the dual-stator induction machine (DSIM) consists of two sets of stator winding on the same stator core [18]. Although DSIM is similar to BDFG in the stator structure, DSIM has a squirrel-cage rotor. Different rotor structures in two types of machines lead to different mathematical models and operating principles. Hence, the DSIM is not concerned in this article.

With the increase in the proportion of wind energy, the research has become a hot topic on how to accurately control the wind turbines to ensure the output power quality of generators meets the grid standards, so more accuracy model and efficient control technology of BDFG must be studied. In [19], the *d-q* model was proposed for BDFG to reduce the model order and was used for the dynamic performance and steady-state analysis. A generalized vector model for BDFG was derived in the rotor reference frame [20] by vector transformations of a coupled circuit model and was used for dynamic performance prediction. For the control technology of BDFIG, a computationally complex method for the rotor flux orientation vector control (VC) based on a dual synchronous coordinate system was proposed in [21]. Poza *et al.* [22] designed a controller based on the PW magnetic flux orientation. However, this method requires multiple proportional integration (PI) controllers and complex decoupling compensation. A simplified VC with the PI controller based on a PW magnetic flux orientation was proposed in [23], which has a good control performance, but the dynamic response of the controller is slightly slower due to the fact that the cross-coupling terms are not considered. The BDFIG direct power control (DPC) and direct torque control technology has a fast dynamic response but the switching harmonics are abundant [24], [25]. The model predictive power control techniques are also applied to BDFIG, improving the dynamic response without cascaded control and modulation [26].

Due to the presence of different types of power electronic equipment, the grid voltage is likely to be unbalanced and even distorted in actual grid conditions. And the DFIG system may be vulnerable due to the connection of stator winding to the network. When the grid is unbalanced, there is an imbalance in the current of the generator set, resulting in the severe heating of the winding and oscillation of torque and output power. In order to solve these problems, a large number of studies have been done to investigate the dynamic behavior and develop control strategies for DFIG under asymmetrical faults [27]–[31]. A feedforward current references control method was proposed in [27] to improve the transient performance of the DFIG system under grid faults. Dual PI current controllers were adopted in [28], including the positive-sequence and negative-sequence current controllers. However, the decomposition process of the positive-sequence and the negative-sequence component increases the computational burden and decreases the dynamic response of the control system. A PI plus resonant current controller in a positive synchronous reference frame was used in [29] and [30]. Although the decomposition process is omitted, the stator flux synchronization of the control scheme needs to be solved. Nian and Song [31] proposed the DPC with PI regulator with faster dynamic response and better robustness under the distorted grid. However, the control accuracy of DPC is low and the power filter is difficult to design.

For optimizing the control of machines under the unbalanced network, although there are many research works on DFIG, there are several research works on BDFIG. For the BDFIG operation under the unbalanced network, Shao *et al*. [32] adopted VC with dual PI controllers, which achieves the active and reactive power generation by adjusting the positive-sequence component, three different control targets by adjusting the negative-sequence component, but the band-trap filter reduces the system dynamic performance. Chen *et al.* [33] adopted the PI plus resonant controller under a single synchronous rotating frame (SRF), the dynamic performance is fast but there is a certain steady-state error because the gain of resonant control cannot be infinitely large. An indirect torque control algorithm for BDFIG under an unbalanced power grid was described in [34] with fewer tuning-demanding elements. An improved DPC algorithm with two hysteresis controllers was presented in [24] to achieve the balanced stator current under unbalanced grid conditions. But much higher frequencies are needed in hysteresis controllers compared with constant switching frequency algorithms. Studies on BDFIG under unbalanced grids were not adequate, more research works need to be done.

Under the unbalanced grid conditions, the accurate control of positive-sequence and negative-sequence CW current is the key to achieve the proposed control targets. This article proposes a dual SRF current control method, which can effectively alleviate the problems of power oscillation and current distortion. The steady-state and dynamic response of the control strategy is satisfactory. In comparison with Shao *et al*. [32], dual SRF current control of the BDFIG system provides a reactive power oscillation suppression target that is not considered in [32]. In addition, the signals' filtering problem in the positive-sequence current control can be eliminated in the proposed control strategy. Compared with Chen *et al*. [33], the zero steady-state error control can be realized by the PI controllers of the proposed control algorithm since the gain of the resonant control in [33] cannot be infinitely large. Compared with the control method in [34], the proposed control algorithm can reduce control complexity and parameter dependence. In contrast to the control strategy adopted in [24], the constant switching frequency for the machine-side converter (MSC) can be ensured in the proposed control strategy. The main contributions of this article are as follows.

1) In the proposed dual SRF current control method, the CW current control strategy is composed of a primary controller and a secondary controller. The primary controller is implemented in the positive-sequence SRF to ensure the dynamic response of the system without the sequence components separation, while the secondary controller is implemented in the negative-sequence SRF and only controls the negative-sequence current components. Compared with the traditional dual PI controllers, the dynamic response and stability of the system are better since the control scheme does not require the positive-sequence components separation.
2) A complete model of the CW negative-sequence current loop is established. Based on the complete model, feedforward compensation terms are added, which equivalently simplify the actual control plant in the negative-sequence SRF, and a simple and effective negative-sequence feedforward current controller is designed. The negative-sequence feedforward current controller effectively reduces the influence of sequence components separation on the dynamic response of the secondary controller.
3) The experimental results not only prove that the proposed control strategy is effective in suppressing the power oscillation and current distortion of the BDFIG system under the unbalanced network but also show that compared with the conventional dual PI current controller, the proposed controller can speed up the dynamic response of the current controller, achieving the control targets quickly.

The structure of this article is as follows. Section II describes the system structure of BDFIG and the principle of variable-speed constant-frequency power generation. In Section III, the dynamic model of BDFIG in the balanced and unbalanced grids is introduced. Section IV designs the control scheme of the CW current in the balanced and unbalanced grids and proposes the feedforward compensation of the negative-sequence current and four control targets under unbalanced grids. The design process

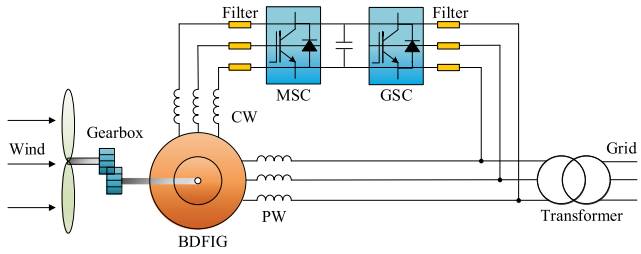

Fig. 1. Topology of BDFIG WPGS.

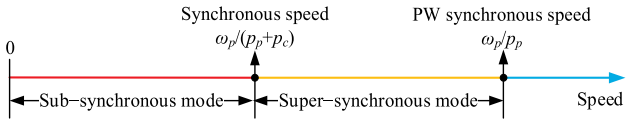

Fig. 2. Operation modes of BDFIG under different speeds.

of the PI controller and robustness analysis under the speed change and parameters variation of the inner current controller are also involved. In Section V, the control structure of the whole system is described. In Section VI, the experimental results of the brushless doubly fed wind power system validate the effectiveness of the proposed control scheme. Finally, the conclusion is given in Section VII.

II. System Configuration

The BDFIG-based wind power system topology is shown in Fig. 1, consisting of two sets of winding on the stator, i.e., the PW and CW. The PW is directly connected to the power grid, and the CW is connected to the back-to-back converter with partly rated power. And, the back-to-back converter comprises the MSC and the grid-side converter (GSC). This configuration greatly reduces the power required for the converter.

When PW and CW are powered, respectively, BDFIG operates in the doubly fed mode. When the PW is powered by the grid and its frequency remains constant, the rotor shaft speed is decided by the CW excitation frequency, as given by

$$n_r = \frac{60\,(f_p + f_c)}{p_p + p_c}. \tag{1}$$

When the rotor speed n_r changes, the current frequency f_c of the CW can be adjusted to keep the output voltage frequency f_p of the PW constant by controlling the power converter, thereby achieving variable-speed constant-frequency power generation. When CW is connected to the dc power, the BDFIG is in the synchronous mode. The speed n_N at this time is called the synchronous speed, which can be expressed by

$$n_N = \frac{60 f_p}{p_p + p_c}. \tag{2}$$

When the rotor speed is slower than the synchronous speed, the BDFIG operates at the subsynchronous mode. Likewise, when the speed exceeds the synchronous speed, the BDFIG operates at the super-synchronous mode, as illustrated in Fig. 2.

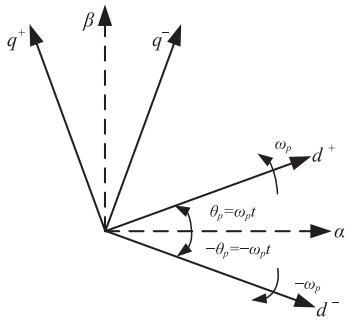

Fig. 3. Transformation relationships between different reference frames.

III. Dynamic Model of the BDFIG System

A. Balanced Grid Condition

If the *d*-axis of the synchronous rotating coordinate system is oriented to the PW stator flux linkage, the vector model of BDFIG [10], [23], [32] can be expressed as

$$\begin{cases} \boldsymbol{u}_{ps} = R_{ps}\boldsymbol{i}_{ps} + \left(\frac{d}{dt} + j\omega_p\right)\boldsymbol{\psi}_{ps} \\ \boldsymbol{u}_{cs} = R_{cs}\boldsymbol{i}_{cs} + \left(\frac{d}{dt} + j\omega_c\right)\boldsymbol{\psi}_{cs} \\ 0 = R_r\boldsymbol{i}_r + \left(\frac{d}{dt} + j\omega_s\right)\boldsymbol{\psi}_r \end{cases} \tag{3}$$

$$\begin{cases} \boldsymbol{\psi}_{ps} = L_{ps}\boldsymbol{i}_{ps} + L_{mp}\boldsymbol{i}_r \\ \boldsymbol{\psi}_{cs} = L_{cs}\boldsymbol{i}_{cs} - L_{mc}\boldsymbol{i}_r \\ \boldsymbol{\psi}_r = L_{mp}\boldsymbol{i}_{ps} - L_{mc}\boldsymbol{i}_{cs} + L_r\boldsymbol{i}_r \end{cases} \tag{4}$$

where

$$\begin{cases} \omega_{\boldsymbol{s}} = \omega_p - p_p\Omega_m \\ \omega_{\boldsymbol{c}} = \omega_p - (p_p + p_c)\Omega_m. \end{cases} \tag{5}$$

And, the active and reactive power of PW can be expressed as

$$\begin{cases} P_p = \frac{3}{2}\mathrm{Re}\left\{\boldsymbol{u}_{ps}\hat{\boldsymbol{i}}_{ps}\right\} \\ Q_p = \frac{3}{2}\mathrm{Im}\left\{\boldsymbol{u}_{ps}\hat{\boldsymbol{i}}_{ps}\right\} \end{cases} \tag{6}$$

where $\hat{\boldsymbol{i}}_{ps}$ represents the conjugation of $\boldsymbol{i}_{ps}$.

B. Unbalanced Grid Condition

When the power grid of the three-phase three-wire system is unbalanced, according to the symmetrical component method, the voltage and current can be decomposed into the positive-sequence component and negative-sequence component, which can be expressed in the stationary ($\alpha\beta$) reference frame as

$$F_{\alpha\beta} = |F_{\alpha\beta+}|\, e^{j\omega_p t} + |F_{\alpha\beta-}|\, e^{-j\omega_p t}. \tag{7}$$

To understand the voltage imbalance degree, the voltage unbalance factor (VUF) is defined as

$$\mathrm{VUF} = \frac{|F_{\alpha\beta-}|}{|F_{\alpha\beta+}|} \times 100\%. \tag{8}$$

Under the unbalanced grid condition, in order to facilitate the analysis of BDFIG, the BDFIG was modeled in a positive-sequence SRF and a negative-sequence SRF. The spatial relationship of each reference coordinate system is shown in Fig. 3.

The d^+-axis of the positive-sequence SRF is oriented to the stator flux of the positive sequence and rotates at an angular velocity ω_p, while the d^--axis of the negative-sequence SRF is oriented to the negative-sequence stator flux, rotating at angular velocity $-\omega_p$.

According to Fig. 3, the transformation relationships between different coordinate systems of the vector *F* are

$$F_{dq}^{+} = F_{\alpha\beta} \cdot e^{-j\omega_p t} \tag{9}$$

$$F_{dq}^{-} = F_{\alpha\beta} \cdot e^{j\omega_p t} \tag{10}$$

$$F_{dq}^{+} = F_{dq}^{-} \cdot e^{-j2\omega_p t} \tag{11}$$

where superscripts "+/−" represent the positive-sequence dq^+ and negative-sequence dq^- reference coordinate systems, respectively.

When the power grid is unbalanced, the electromagnetic vector (current, voltage, flux linkage, etc.) can be decomposed into the positive- and negative-sequence components. The electromagnetic vector *F* in the dq^+ coordinate system is expressed by the positive and negative-sequence components as

$$F^{+} = F_{+}^{+} + F_{-}^{-} e^{-j2\omega_p t} \tag{12}$$

where subscripts "+/−" represent the positive- and negative-sequence components, respectively. The negative-sequence component rotates at twice the PW fundamental frequency relative to the positive-sequence component. This formula applies to the stator and rotor winding, which is denoted as

$$\begin{cases} F_p^{+} = F_{p+}^{+} + F_{p^-}^{-} e^{-j2\omega_p t} \\ F_c^{+} = F_{c+}^{+} + F_{c^-}^{-} e^{-j2\omega_p t} \\ F_r^{+} = F_{r+}^{+} + F_{r^-}^{-} e^{-j2\omega_p t} \end{cases} \tag{13}$$

In summary, the mathematical model considering the positive- and negative-sequence components of BDFIG is expressed as follows.

The voltage equation is denoted as

$$\begin{cases} \boldsymbol{u}_{ps+}^{+} = R_{ps}\boldsymbol{i}_{ps+}^{+} + \left(\frac{d}{dt} + j\omega_p\right)\boldsymbol{\psi}_{ps+}^{+} \\ \boldsymbol{u}_{cs+}^{+} = R_{cs}\boldsymbol{i}_{cs+}^{+} + \left(\frac{d}{dt} + j\omega_c\right)\boldsymbol{\psi}_{cs+}^{+} \\ \boldsymbol{u}_{r+}^{+} = R_r\boldsymbol{i}_{r+}^{+} + \left(\frac{d}{dt} + j\omega_s\right)\boldsymbol{\psi}_{r+}^{+} \end{cases} \tag{14}$$

$$\begin{cases} \boldsymbol{u}_{ps-}^{-} = R_{ps}\boldsymbol{i}_{ps-}^{-} + \left(\frac{d}{dt} - j\omega_p\right)\boldsymbol{\psi}_{ps-}^{-} \\ \boldsymbol{u}_{cs-}^{-} = R_{cs}\boldsymbol{i}_{cs-}^{-} + \left(\frac{d}{dt} + j\left(\omega_c - 2\omega_p\right)\right)\boldsymbol{\psi}_{cs-}^{-} \\ \boldsymbol{u}_{r-}^{-} = R_r\boldsymbol{i}_{r-}^{-} + \left(\frac{d}{dt} + j\left(\omega_s - 2\omega_p\right)\right)\boldsymbol{\psi}_{r-}^{-}. \end{cases} \tag{15}$$

The active and reactive power can be expressed as

$$\begin{cases} P_p = \frac{3}{2}\mathrm{Re}\left\{\boldsymbol{u}_{ps}^{+}\overset{\wedge}{\boldsymbol{i}}_{ps}^{+}\right\} \\ = \frac{3}{2}\mathrm{Re}\left\{\left(\boldsymbol{u}_{ps+}^{+} + \boldsymbol{u}_{ps-}^{-}e^{-j2\omega_p t}\right)\cdot\left(\hat{\boldsymbol{i}}_{ps+}^{+} + \hat{\boldsymbol{i}}_{ps-}^{-}e^{j2\omega_p t}\right)\right\} \\ = P_{p0} + P_{p\cos 2}\cos\left(2\omega_p t\right) + P_{p\sin 2}\sin\left(2\omega_p t\right) \\ Q_p = \frac{3}{2}\mathrm{Im}\left\{\boldsymbol{u}_{ps}^{+}\overset{\wedge}{\boldsymbol{i}}_{ps}^{+}\right\} \\ = \frac{3}{2}\mathrm{Im}\left\{\left(\boldsymbol{u}_{ps+}^{+} + \boldsymbol{u}_{ps-}^{-}e^{-j2\omega_p t}\right)\cdot\left(\hat{\boldsymbol{i}}_{ps+}^{+} + \hat{\boldsymbol{i}}_{ps-}^{-}e^{j2\omega_p t}\right)\right\} \\ = Q_{p0} + Q_{p\cos 2}\cos\left(2\omega_p t\right) + Q_{p\sin 2}\sin\left(2\omega_p t\right) \end{cases} \tag{16}$$

where

$$\begin{bmatrix} P_{p0} \\ Q_{p0} \\ P_{p\cos 2} \\ P_{p\sin 2} \\ Q_{p\cos 2} \\ Q_{p\sin 2} \end{bmatrix} = \frac{3}{2} \begin{bmatrix} u^+_{psd+} & u^+_{psq+} & u^-_{psd-} & u^-_{psq-} \\ u^+_{psq+} & -u^+_{psd+} & u^-_{psq-} & -u^-_{psd-} \\ u^-_{psd-} & u^-_{psq-} & u^+_{psd+} & u^+_{psq+} \\ u^-_{psq-} & -u^-_{psd-} & -u^+_{psq+} & u^+_{psd+} \\ u^-_{psq-} & -u^-_{psd-} & u^+_{psq+} & -u^+_{psd+} \\ -u^-_{psd-} & -u^-_{psq-} & u^+_{psd+} & u^+_{psq+} \end{bmatrix} \times \begin{bmatrix} i^+_{psd+} \\ i^+_{psq+} \\ i^-_{psd-} \\ i^-_{psq-} \end{bmatrix}. \tag{17}$$

IV. System Control Scheme

A. Balanced Grid Condition

Under balanced grid conditions, since the d-axis of SRF is oriented to the PW stator flux, PW flux can be expressed as

$$\boldsymbol{\psi}_{ps} = \psi_{psd} + j\psi_{psq} = \psi_{psd}. \tag{18}$$

During the normal operation of BDFIG, the grid voltage is basically constant. According to (3), assuming R_{ps} and u_{psd} approximately equal to zero, power equation (6) can be simplified as

$$\begin{cases} P_p = \frac{3}{2}\left(u_{psd}i_{psd} + u_{psq}i_{psq}\right) \approx \frac{3}{2}u_{psq}i_{psq} \\ Q_p = \frac{3}{2}\left(u_{psq}i_{psd} - u_{psd}i_{psq}\right) \approx \frac{3}{2}u_{psq}i_{psd}. \end{cases} \tag{19}$$

Equation (19) shows that the active and reactive power of the stator can be independently controlled by adjusting the q-axis and d-axis current of the PW, respectively. However, since the PW is directly connected to the power grid, it cannot be controlled directly and the PW current can be controlled indirectly by adjusting the CW current. According to (3) and (4), the relationship between the PW and CW current described in the form of a complex transfer function can be obtained as

$$\boldsymbol{i}_{ps}(s) = -k(1 + G_r(s))\boldsymbol{i}_{cs}(s) + \frac{1 + (s + j\omega_s)T_r}{1 + (s + j\omega_s)T_r{}'} \frac{\boldsymbol{\psi}_{ps}(s)}{L_{ps}} \tag{20}$$

where $k = L_{mp}L_{mc}/(L_{ps}L_r{}')$, $T_r = L_r/R_r$, $T_r{}' = L_r{}'/R_r$, $L_r{}' = L_r – L_{mp}{}^2/L_{ps}$, and

$$G_r(s) = -\frac{1}{1 + (s + j\omega_s)T_r{}'}. \tag{21}$$

The first term in (20) shows that the PW current can be controlled by CW and the second term is a constant disturbance term. The cross coupling between the d and q axes of the PW current as well as the disturbance term of the magnetic flux can be compensated by the PI controllers to achieve a decoupling control of the active and reactive power.

Ignoring the rotor resistance R_r can simplify the control method [10]. In this case, the rotor transient time constant T_r' tends to be infinite and $G_r(s)$ is close to zero, so (20) can be simplified as

$$\boldsymbol{i}_{ps}(s) = -k\boldsymbol{i}_{cs}(s) + k_1\frac{\boldsymbol{\psi}_{ps}(s)}{L_{ps}} \tag{22}$$

TABLE I
PI Parameters of Controllers

PI Parameters	Positive sequence SRF		Negative sequence SRF
	Outer power loop	Inner current loop	Negative sequence current loop
k_p	3.26 ($0.1k_i$)	36 ($g_2 \times L_{sc}$)	36 ($g_3 \times L_{sc}$)
k_i	32.6 (g_1/k)	255 ($g_2 \times R_{sc}$)	255 ($g_3 \times R_{sc}$)
	$k = \frac{L_{mp}L_{mc}}{L_{ps}L_r{}'}$	$g_1 = 30$	$g_2 = g_3 = 200$

where $k_1 = L_r/L_r{}'$.

Since the second term in (22) is a disturbance term, it can be ignored in the PI controller design, so the transfer function $G_s(s)$ from $\boldsymbol{i_c}$ to $\boldsymbol{i_p}$ is

$$G_s(s) = -\frac{L_{mp}L_{mc}}{L_{ps}L_r{}'}. \tag{23}$$

The PI controller design method for a typical first-order system was given in [35], which is called the pole-zero cancellation. The PI controller can be expressed as

$$F(s) = \frac{g_1}{s}\left|G_s^{-1}(s)\right| = k_p + \frac{k_i}{s} \tag{24}$$

where g_1 is controller gain, which is set to the desired closed-loop system bandwidth, and $k_p = 0$ and $k_i = g_1 \times L_{ps}L_r{}'/(L_{mp}L_{mc})$. Considering that $G_r(s)$ is merely close to zero, k_p is set as $0.1k_i$, the specific values can be seen in Table I. In this situation, the zero point of the PI controller can offset the pole point of the transfer function. The closed-loop system bandwidth and response time (10%–90%) [35] are g_1 rad/s and (ln9/g_1) s, respectively. Taken the system bandwidth and response time into account, controller gain g_1 is set as 30.

According to (4), the magnetic flux of CW can be expressed as

$$\boldsymbol{\psi_{cs}} = L_{cs}\boldsymbol{i}_{cs} + L_{ps}\frac{L_{mc}}{L_{mp}}\boldsymbol{i}_{ps} - \frac{L_{mc}}{L_{mp}}\boldsymbol{\psi_{ps}}. \tag{25}$$

The control voltage equation of CW can be obtained from (3) and (22), which is given by

$$\begin{aligned} \boldsymbol{u}_{cs}(s) = {} & (R_{cs} + sL_{cs})\boldsymbol{i}_{cs}(s) + k_2(s + j\omega_c)L_{ps}\boldsymbol{i}_{ps}(s) \\ & + j\omega_c L_{cs}\boldsymbol{i}_{cs}(s) - k_2(s + j\omega_c)\psi_{ps}(s) \end{aligned} \tag{26}$$

where $k_2 = L_{mc}/L_{mp}$. The first term realizes the decoupling control between the CW voltage and current, and the second to fourth terms are the compensation terms to speed up the dynamic response.

Considering (20) and (26), a double closed-loop control system can be designed. The outer loop is called the power loop, and the PI controller outputs the reference value of CW current $\boldsymbol{i}_{cs}{}^*$. The inner loop is the current loop, which generates the CW control voltage reference $\boldsymbol{u}_{cs}{}^*$. The schematic diagram is shown in Fig. 4. From (26), the equivalent transfer function G_c(s) [37]

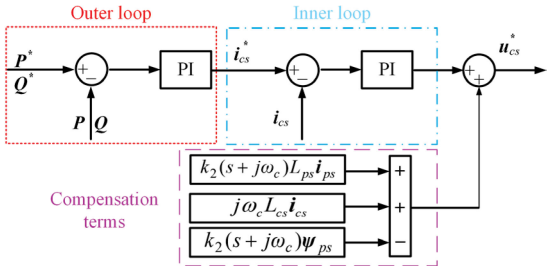

Fig. 4. Schematic diagram of double closed-loop control.

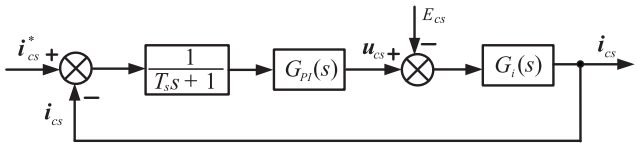

Fig. 5. Control block of the inner current loop.

from $\boldsymbol{u}_{cs}$ to $\boldsymbol{i}_{cs}$ is expressed as

$$G_c(s) = \frac{1}{R_{cs} + sL_{cs}}. \tag{27}$$

According to the pole-zero cancellation, the PI parameters of the inner current loop are set as $k_p = g_2 \times L_{cs}$ and $k_i = g_2 \times R_{cs}$. Taken the system bandwidth and response time into account, controller gain g_2 is set as 200, the specific values can be seen in Table I.

B. Robustness Analysis Under Speed Change and Parameters Variation of Inner Current Controller

Based on (20), (22), and (26), (26) can be deduced as

$$\begin{aligned} \boldsymbol{u}_{cs}(s) =& \left(\left(L_{cs} - kk_2\left(1+G_r\right)L_{ps}\right)(s+j\omega_c) + R_{cs}\right)\boldsymbol{i}_{cs}(s) \\ &+ j\omega_c k_2\left(k_1 - 1\right)\boldsymbol{\psi}_{ps}(s) \\ =& \frac{1}{G_i(s)} \cdot \boldsymbol{i}_{cs}(s) + E_{cs} \end{aligned} \tag{28}$$

where E_{cs} is treated as the disturbance to the inner current loop. Based on (28), the control loop of the inner current is shown in Fig. 5. $G_{\mathrm{PI}}(s)$ represents the transfer function of the PI controller, and $1/(T_s s+1)$ is the sampling and computing delay. The closed-loop transfer function of the inner current loop can be given by

$$\begin{aligned} G(s) &= \frac{G_{\mathrm{PI}}(s) \cdot G_i(s)/(T_s s+1)}{1 + G_{\mathrm{PI}}(s) \cdot G_i(s)/(T_s s+1)} \\ &= \frac{G_{\mathrm{PI}}(s) \cdot G_i(s)}{(T_s s+1) + G_{\mathrm{PI}}(s) \cdot G_i(s)}. \end{aligned} \tag{29}$$

The rotor speed and parameters variation may affect the stability of the proposed control strategies. The BDFIG system has the operation range centered ±33% around the synchronous speed n_N [8], which is corresponding to the normal speed range (0.67–1.33n_N) in this article. A higher dc-link voltage and converter capacity are required for a larger speed range. Correspondingly,

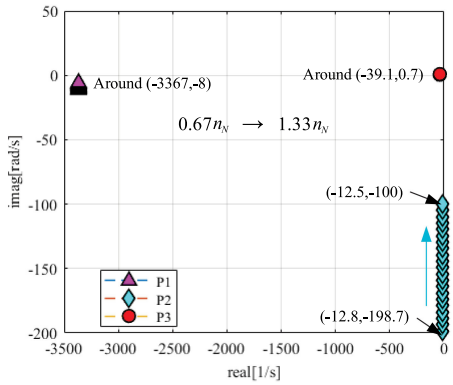

Fig. 6. Root locus diagrams of the inner current controller when the rotor speed changes from 0.67n_N to 1.33n_N.

the BDFIG system will lose the low-cost advantage. Therefore, only the speed range from 0.67n_N to 1.33n_N is considered in this article.

The root locus diagram of the inner current controller under the speed range (0.67–1.33n_N) is illustrated in Fig. 6, where one pole in each pair is shown. The location of pole 1 changes slightly, the location of pole 2 changes along the parallel direction of the image axis, and the location of pole 3 remains unchanged. The locations of three poles are all in the left plane, which shows good robustness when the rotor speed changes from 0.67n_N to 1.33n_N.

In the inner current loop, the control stability will also be affected by the parameters variation of R_{cs} and L_{cs}. Considering the practical operating conditions of the BDFIG, L_{cs} is mainly affected by the saturation of the iron core. Assume that L_{cs} changes from L_{csN} to 0.6L_{csN} when the degree of saturation increases, where L_{csN} is the unsaturated self-inductance of CW. R_{cs} is mainly affected by temperature. Assume that R_{cs} changes from R_{csN} to 1.2R_{csN} when the machine temperature increases, where R_{csN} is the cold-state resistance.

In order to analyze the stability of the inner current loop, the root locus diagrams under parameters variation are shown in Fig. 7, where one pole in each pair is shown, and the shaft speed is 1.33n_N. It can be seen from Fig. 7(a) that when L_{cs} changes from L_{csN} to 0.6L_{csN}, the location of pole 1 changes a little, and the locations of poles 2 and 3 vary to a slight extent. From Fig. 7(b), when R_{cs} changes from R_{csN} to 1.2R_{csN}, the locations of three poles almost remain unchanged. All the poles in Fig. 7(a) and (b) stay on the left side of the plane, which shows that the robustness of the inner current controller is good under parameters variation.

C. Unbalanced Grid Condition

In order to adjust the positive- and negative-sequence components of the CW current, respectively, it is traditional to use the positive-sequence controller in the dq^+ coordinate system for controlling the positive-sequence current component and the negative-sequence controller in the dq^- coordinate system for controlling the negative-sequence current component.

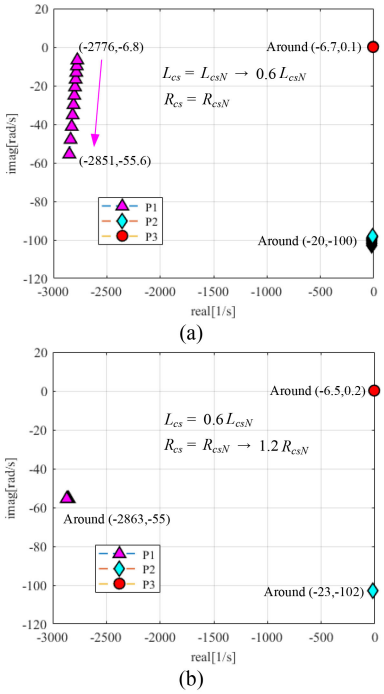

Fig. 7. Root locus diagrams of the inner current controller under parameters variation. (a) L_{cs} changes from L_{csN} to $0.6L_{csN}$. (b) R_{cs} changes from R_{csN} to $1.2R_{csN}$.

Therefore, both positive- and negative-sequence components must be decomposed from the electromagnetic vector. Because the extraction process of the positive- and negative-sequence components has a considerable delay and introduces errors into the signal, the dynamic performance and stability of the system will be reduced. In addition, even in the case of a balanced grid, the control system still needs sequence components separation, which undoubtedly affects the dynamic performance of the entire system.

To address these issues, current control strategies, including a primary controller and a secondary controller, are used. The primary controller is implemented in the positive-sequence SRF without the sequence components separation. The primary controller directly controls the current in the positive-sequence SRF to ensure the stability and dynamic response of the system. The secondary controller is implemented in the negative-sequence SRF and only controls the extracted negative-sequence current components.

Based on (26), under the unbalanced network, the CW voltage equation can be expressed in the positive-sequence SRF as

$$\boldsymbol{u}_{cs}^{+}(s) = (R_{cs} + sL_{cs})\boldsymbol{i}_{cs}^{+}(s) + k_2(s + j\omega_c)L_{ps}\boldsymbol{i}_{ps}^{+}(s) + j\omega_c L_{cs}\boldsymbol{i}_{cs}^{+}(s) - k_2(s + j\omega_c)\boldsymbol{\psi}_{ps}^{+}(s). \quad (30)$$

Substituting (12) into (30) and splitting yield the CW voltage equation of the primary and secondary controllers, which are, respectively, given as follows:

$$\boldsymbol{u}_{cs+}^{+}(s) = (R_{cs} + sL_{cs})\,\boldsymbol{i}_{cs+}^{+}(s) + j\omega_c k_2 L_{ps}\boldsymbol{i}_{ps}^{+}(s) + j\omega_c L_{cs}\boldsymbol{i}_{cs}^{+}(s) - j\omega_c k_2\boldsymbol{\psi}_{ps}^{+}(s) \quad (31)$$

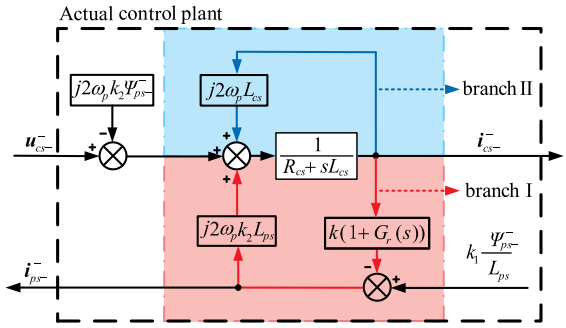

Fig. 8. Negative-sequence current loop structure.

$$\boldsymbol{u}_{cs-}^{-}(s) = (R_{cs} + sL_{cs})\,\boldsymbol{i}_{cs-}^{-}(s) - j2\omega_p L_{cs}\boldsymbol{i}_{cs-}^{-}(s) - j2\omega_p k_2 L_{ps}\boldsymbol{i}_{ps-}^{-}(s) + j2\omega_p k_2\boldsymbol{\psi}_{ps-}^{-}(s). \quad (32)$$

The entire CW control voltage is the sum of the output of the primary controller and the secondary controller, so the total CW control voltage in the positive-sequence SRF is given by

$$\boldsymbol{u}_{cs}^{+} = \boldsymbol{u}_{cs+}^{+} + \boldsymbol{u}_{cs-}^{-}e^{-j2\omega_p t}. \quad (33)$$

D. Feedforward Compensation for Negative-Sequence Current Control

The dynamic response of the negative current controller may be influenced by the decomposition process of voltage and current. In order to improve this situation, the feedforward compensation for the negative-sequence current control is adopted [37].

Based on (32), the negative-sequence current loop model can be expressed as

$$(R_{cs} + sL_{cs})\,\boldsymbol{i}_{cs-}^{-}(s) = \boldsymbol{u}_{cs-}^{-}(s) + j2\omega_p L_{cs}\boldsymbol{i}_{cs-}^{-}(s) + j2\omega_p k_2 L_{ps}\boldsymbol{i}_{ps-}^{-}(s) - j2\omega_p k_2\psi_{ps-}^{-}(s). \quad (34)$$

According to (34), the negative-sequence current loop structure is illustrated in Fig. 8. The first-order inertia link $G_{RL}(s) = 1/(R_{cs}+sL_{cs})$ is the core of the current inner loop. The CW current $\boldsymbol{i}_{cs-}^{-}$ has two feedback branches, where branch I passes the intermediate variable PW current $\boldsymbol{i}_{ps-}^{-}$ and branch II is feedback to the input voltage through the term $j2\omega_p L_{cs}$.

In the negative-sequence current loop structure, as shown in Fig. 8, the feedback branch I is composed of two series links, which is too complicated to be a feedforward term. If the term $j2\omega_p k_2 L_{ps}\boldsymbol{i}_{ps-}^{-}$ is selected as the feedforward term, it can equivalently "cuts off" branch I and thus equivalently simplifies the structure of the current loop. The corresponding controller structure is shown in Fig. 9 and the block $1/(T_s s+1)$ is the sampling and computing delay. In addition, the current feedforward term $j2\omega_p L_{cs}\boldsymbol{i}_{cs-}^{-}$ can directly offset the feedback branch II, and the magnetic flux feedforward term $j2\omega_p k_2\psi_{cs-}^{-}$ can compensate for the influence of the back electromotive force component. The final control plant can be equivalent to the first-order inertia link $G_{RL}(s)$, which is illustrated in Fig. 10. Based on the classic control theory, both the bias term and feedforward term for ψ_{ps} are converted into the dc disturbance $\boldsymbol{E}_{phi\_ps}$.

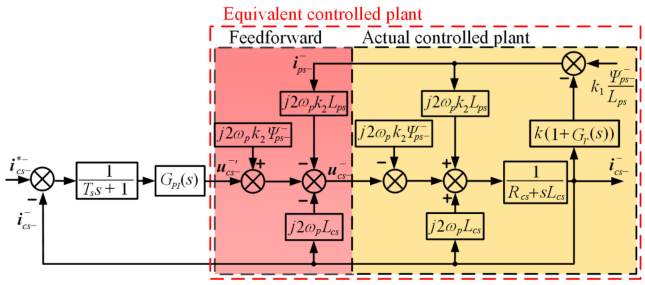

Fig. 9. Negative-sequence current feedforward controller.

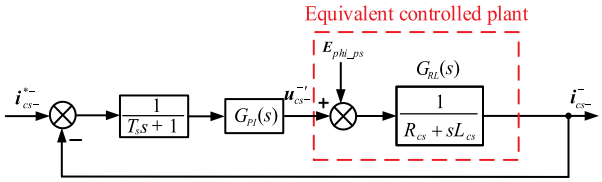

Fig. 10. Equivalent control block diagram of the negative-sequence current controller.

For the corresponding PI controller, the pole-zero cancellation method can be used to set the PI parameters: set k_p to $g_3 \times L_{cs}$ and k_i to $g_3 \times R_{cs}$. Taken the system bandwidth and response time into account, controller gain g_3 is set as 200. The specific values of the PI controller can be seen in Table I.

E. Control Targets

Under the unbalanced grid condition, both positive- and negative-sequence currents need to be controlled in order to suppress the active and reactive power ripple and improve the output current quality. In addition to controlling the average stator active power P_{p0} and reactive power Q_{p0}, two other parameters can be controlled, i.e., PW current $\boldsymbol{i}_{ps}$ and CW current $\boldsymbol{i}_{cs}$. Four different control targets are proposed as follows.

Target I: Active power ripple cancellation. In this case, there is no 100 Hz power oscillation in the active power of the PW. If $P_{p\cos 2} = P_{p\sin 2} = 0$, the PW current command is expressed as

$$\begin{cases} i_{psd-}^{-*} = \dfrac{1}{u_{psq+}^{+}} \left(u_{psq-}^{-} i_{psd+}^{+} - u_{psd-}^{-} i_{psq+}^{+} \right) \\ i_{psq-}^{-*} = -\dfrac{1}{u_{psq+}^{+}} \left(u_{psd-}^{-} i_{psd+}^{+} + u_{psq-}^{-} i_{psq+}^{+} \right). \end{cases} \tag{35}$$

Target II: Reactive power ripple suppression. In this case, there will be no double frequency power oscillation in the reactive power of the PW. If $Q_{p\cos 2} = Q_{p\sin 2} = 0$, the PW current command is given by

$$\begin{cases} i_{psd-}^{-*} = -\dfrac{1}{u_{psq+}^{+}} \left(u_{psq-}^{-} i_{psd+}^{+} - u_{psd-}^{-} i_{psq+}^{+} \right) \\ i_{psq-}^{-*} = \dfrac{1}{u_{psq+}^{+}} \left(u_{psd-}^{-} i_{psd+}^{+} + u_{psq-}^{-} i_{psq+}^{+} \right). \end{cases} \tag{36}$$

Target III: Balanced PW current. In this case, the negative-sequence current in the PW is suppressed by injecting a negative-sequence current into the CW. The CW current balance is sacrificed to ensure the PW current balance. The PW current

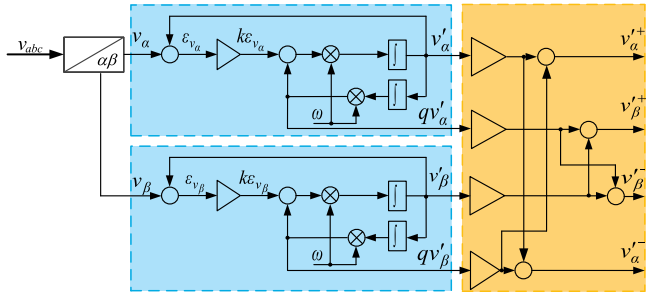

Fig. 11. Structure block diagram of DSOGI.

command is given by

$$\begin{cases} i_{psd-}^{-*} = 0 \\ i_{psq-}^{-*} = 0. \end{cases} \tag{37}$$

Target IV: No CW current oscillation. In this case, the harmonic current in the CW is avoided but the imbalance of the PW current and the power oscillation at 100 Hz still exists. The CW current command is expressed as

$$\begin{cases} i_{csd-}^{-*} = 0 \\ i_{csq-}^{-*} = 0. \end{cases} \tag{38}$$

In addition to the four targets listed above, other targets may also help rebalance the current or reduce power oscillations. In practice, the control targets need to be reasonably selected, or each target can be summed by weight according to actual requirements so that the corresponding problem can be improved to a certain degree.

V. System Implementation

Under the unbalanced grid condition, the stator flux contains positive- and negative-sequence components. In order to achieve precise coordinate system orientation, the phase-locked loop must lock the positive-sequence stator flux linkage. In order to accurately detect the phase angle and angular frequency of the PW stator flux linkage, a phase-locked loop, including band-stop filters, is used.

A. Sequence Components Separation

In the past, when DFIG was operated under the unbalanced grid, a trap filter was used to extract the negative-sequence component but the dynamic response would be greatly reduced. Since the second-order generalized integrator (SOGI) itself is a quadrature signal generator, the instantaneous positive- and negative-sequence components of the three-phase input vector can be obtained by applying the SOGI in the α and β components of the input vector [37]. The implementation structure of the algorithm dual-SOGI (DSOGI) is shown in Fig. 11. This structure can detect the positive- and negative-sequence components of the three-phase input vector at a certain frequency ω and has a high static and dynamic performance. Once the negative-sequence component is obtained by the DSOGI method, it can be converted into a negative-sequence dc component through the corresponding coordinate system transformation.

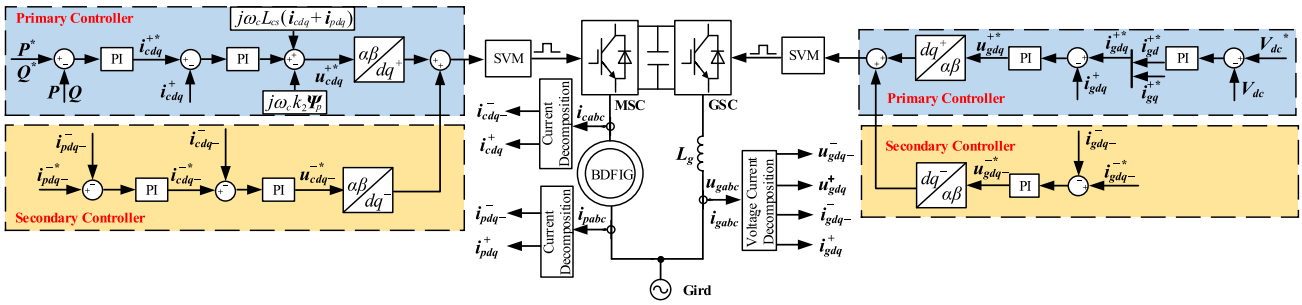

Fig. 12. Schematic diagram of the control system structure.

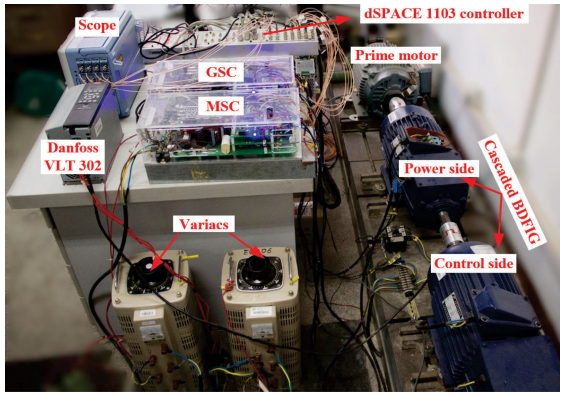

Fig. 13. Topology of the BDFIG system platform.

TABLE II
MACHINE PARAMETERS OF BDFIG

Parameters	Value
Pole pair number of PW p_p	2
Pole pair number of CW p_c	2
Resistance of PW R_{ps}	1.277 Ω
Resistance of CW R_{cs}	1.277 Ω
Resistance of rotor R_r	2.902 Ω
Self−inductance of PW L_{ps}	180.670 mH
Self−inductance of CW L_{cs}	180.670 mH
Self−inductance of rotor L_r	181.67 mH
Magnetizing inductance of PW L_{mp}	177.375 mH
Magnetizing inductance of CW L_{mc}	177.375 mH

B. Control System Structure

Fig. 12 shows a schematic diagram of the entire control system. In order to improve the dynamic performance of the BDFIG system, the unbalance of the grid voltage needs to be detected to determine whether the secondary controller is turned ON. When the VUF exceeds 1%, the secondary controller is turned ON and the positive- and negative-sequence current reference values are generated according to the preselected control target; when VUF is less than 1%, the secondary controller is disabled to guarantee the system dynamic response, only the positive-sequence current reference is generated.

The current reference is then passed to the primary and secondary controllers to generate the required CW control voltage, and then a space vector modulation is used to generate the MSC pulse signal for controlling the BDFIG.

VI. EXPERIMENTAL RESULT

A. Experimental Setup

In order to verify the effectiveness of the proposed control strategy, experimental tests were performed on the cascaded BDFIG system platform, which is illustrated in Fig. 13, and the parameters of the cascaded BDFIG are given in Table II. The BDFIG consists of two identical wound-rotor induction machines and the PW is connected to the grid via two variacs, which can be adjusted to provide balanced and unbalanced grid conditions. The CW is connected to a bidirectional power converter. The BDFIG is driven by an 11-kW induction machine equipped with a converter. An incremental encoder is used to measure the rotor position and speed, and the stator voltage and current are measured by sensors.

The dSPACE 1103 accepts the measurement signal and generates a pulsewidth modulation signal according to the control algorithm to control the bidirectional power converter. The GSC is used to maintain the dc bus voltage stable and the MSC is used to control the BDFIG with 10 kHz sampling frequency.

B. Power Decoupling Control

The power decoupling control experiments of the BDFIG system are first performed for it is the basis for subsequent experiments. Under the subsynchronous speed ($0.8n_N$, 600 r/min), the active power is stepped from 600 to 900 W and then stepped to 750 W. The reactive power is reduced from 600 to 0 var and then raised to 300 var. The experimental results are shown in Fig. 14. It can be seen that the decoupled control of active and reactive power can be achieved through double closed-loop control.

C. Proposed Control Scheme Under Unbalanced Grid Condition

In order to verify the effectiveness of the proposed control strategy under the unbalanced grid, a set of experiments with different control targets is implemented, where VUF is 7%.

The average active power is 500 W and the average reactive power is 0 var. The dynamic performance before and after applying the proposed control strategy under different control targets in the subsynchronous speed ($0.8n_N$, 600 r/min) is shown

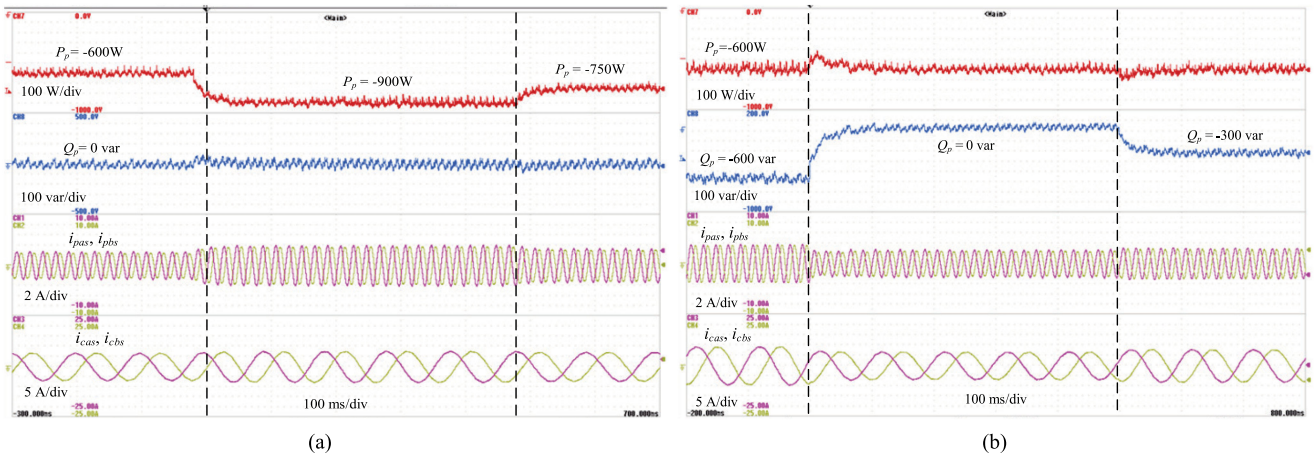

Fig. 14. Experimental results of power decoupling control. (a) Active power step changes. (b) Reactive power step changes.

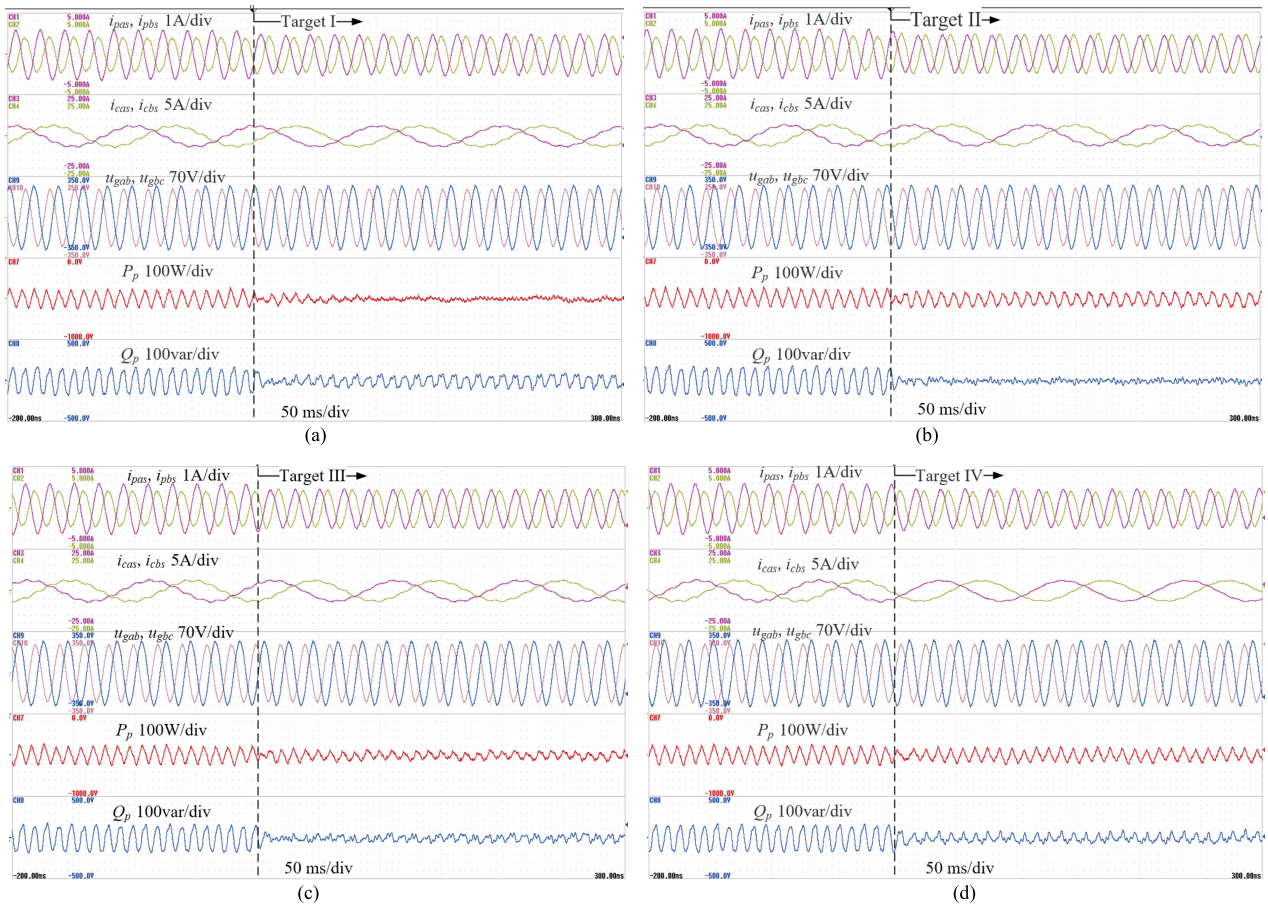

Fig. 15. Experimental waveforms of the BDFIG operation states under different control targets. (a) Control target I for suppressing the active power ripple. (b) Control target II for the reactive power ripple cancellation. (c) Control target III for the PW current balance. (d) Control target IV for the CW current with no oscillation.

in Fig. 15. The waveforms in each figure represent PW phase current (i_{pas} and i_{pbs}), CW phase current (i_{cas} and i_{cbs}), grid line voltage (u_{gab} and u_{gbc}), PW active power P_p, and PW reactive power Q_p. Target I suppresses the active power ripple but a large reactive power ripple can still be observed. Target II suppresses the reactive power ripple at the expense of the active power and stator current fluctuation. Target III obtains a three-phase balanced PW current by restraining the power pulsation and CW current imbalance to a certain degree, and for Target IV, there is no CW current oscillation.

The transient experiments of the BDFIG system between sub-synchronous ($0.8n_N$, 600 r/min) and super-synchronous speed

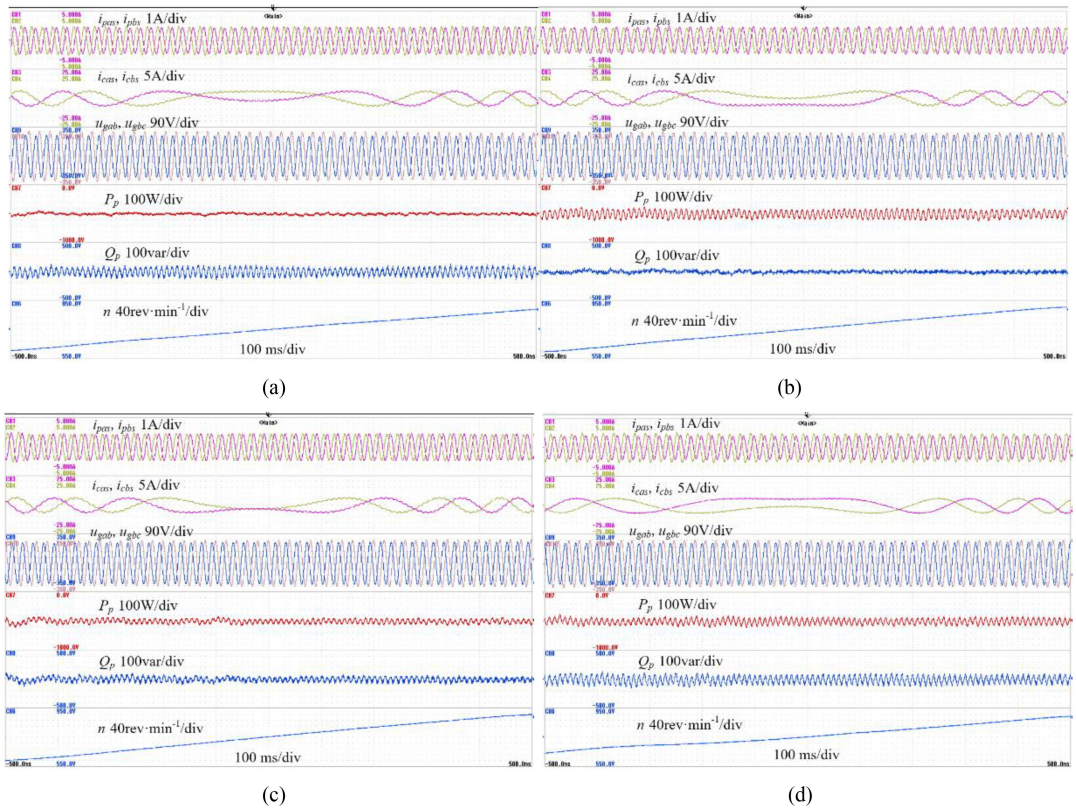

Fig. 16. Transient experiments of the BDFIG system in different control targets under changing rotor speed from subsynchronous ($0.8n_N$, 600 r/min) to super-synchronous speed ($1.2n_N$, 900 r/min) with 7% VUF. (a) Control target I for suppressing the active power ripple. (b) Control target II for the reactive power ripple cancellation. (c) Control target III for the PW current balance. (d) Control target IV for the CW current with no oscillation.

($1.2n_N$, 900 r/min) under 7% VUF are shown in Fig. 16. The average active power and reactive power are set as 500 W and 0 var, respectively. The last waveforms in each figure represent rotor speed n. It can be seen from Fig. 16 that the active power ripple is suppressed in Fig. 16(a), the reactive power ripple is eliminated in Fig. 16(b), the PW current remains balanced in Fig. 16(c), and the CW current maintains sinusoidal in Fig. 16(d) when the rotor speed changes from 600 to 900 r/min. The achievement of the control targets illustrates the effectiveness of the proposed control strategy.

The principle of this control method is to improve the stator current by controlling the positive-sequence and negative-sequence currents of the PW, thus suppressing the power pulsation. The harmonic spectrums of power and current before and after applying the proposed control scheme of Fig. 15 are shown in Fig. 17. It is obvious that before the control strategy is applied, both active and reactive powers oscillate at double PW fundamental frequency with total harmonic distortion (THD) exceeding 20%, while there are harmonics at the frequency of $2\omega_p - \omega_c$ (90 Hz) in the CW current with a THD close to 10%. By using the proposed controller, the active and reactive power oscillations are suppressed and reduced to 5.16% and 4.77%, respectively. The harmonic content of the CW is also reduced, and the THD is reduced to 4.81%. For the PW current, an unbalance degree is the main problem. The unbalance degree of PW current is reduced from 26.09% to 3.5% after the control.

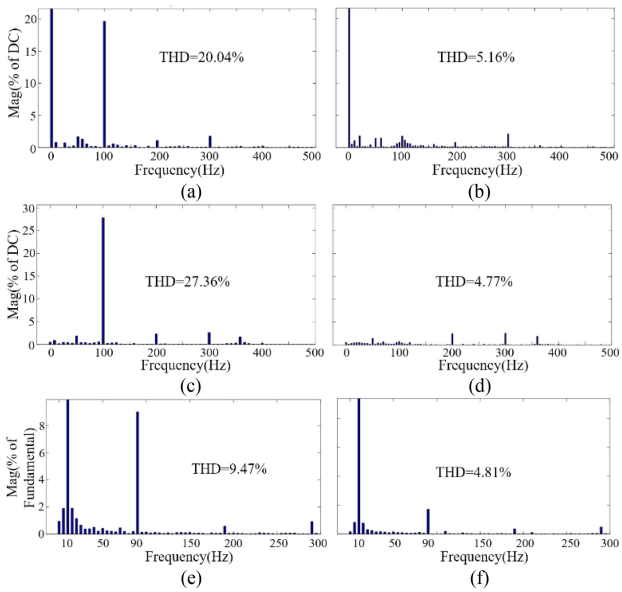

Fig. 17. Harmonic spectrum of power and current before (a), (c), and (e) and after (b), (d), and (f) applying the proposed control scheme. (a) and (b) Active power. (c) and (d) Reactive power. (e) and (f) CW current.

More information about the unbalance degree and THD of active power, reactive power, and CW current can be seen in Table III. Therefore, the comparison in Table III and the results

TABLE III
UNBALANCE DEGREE OR THD OF FOUR TARGETS

Target	Conventional	I	II	III	IV
Active power oscillation	20.04%	**5.16%**	15.93%	9.93%	15.12%
Reactive power oscillation	27.36%	13.21%	**4.77%**	7.71%	9.48%
PW current unbalance	26.09%	9.13%	7.55%	**3.50%**	9.62%
CW current distortion	9.47%	7.19%	8.04%	7.56%	**4.81%**

of Figs. 15–17 prove the effectiveness of the proposed control strategy.

VII. CONCLUSION

This article investigates the modeling and control of BDFIG under the unbalanced network. When the grid is unbalanced, the current of the generator winding will be unbalanced, causing severe heating of the winding and oscillation of torque and output power. To mitigate these problems, this article proposes a dual SRF current control strategy. The controller parameters have been designed and the stability analysis has been conducted. Experiments on a prototype machine verify the effectiveness of the proposed control strategy, drawing the following conclusions.

1) In the proposed dual SRF current control method, the primary controller is implemented in the positive-sequence SRF to ensure the dynamic response without the sequence components separation, while the secondary controller is implemented in the negative-sequence SRF and only controls the negative-sequence current component.
2) The negative-sequence feedforward current controller effectively reduces the influence of sequence components separation on the dynamic response of the secondary controller.
3) The proposed control strategy not only can suppress the power oscillation and current distortion of the BDFIG system under the unbalanced network but also speed up the dynamic response of the current controller and achieve the control targets quickly.

REFERENCES

[1] M. Cheng and Y. Zhu, "The state of the art of wind energy conversion systems and technologies: A review," *Energy Convers. Manage.*, vol. 88, pp. 332–347, Dec. 2014.

[2] Global Wind Energy Council, Global wind 2019 report, Oct. 2019. [Online]. Available: https://gwec.net/global--wind--report--2019/

[3] H. Geng, C. Liu, and G. Yang, "LVRT capability of DFIG-based WECS under asymmetrical grid fault condition," *IEEE Trans. Ind. Electron.*, vol. 60, no. 6, pp. 2495–2509, Jun. 2013.

[4] H. Polinder, J. A. Ferreira, B. B. Jensen, A. B. Abrahamsen, K. Atallah, and R. A. McMahon, "Trends in wind turbine generator systems," *IEEE J. Emerg. Sel. Top. Power Electron.*, vol. 1, no. 3, pp. 174–185, Sep. 2013.

[5] Z. Chen, J. M. Guerrero, and F. Blaabjerg, "A review of the state of the art of power electronics for wind turbines," *IEEE Trans. Power Electron.*, vol. 24, no. 8, pp. 1859–1875, Aug. 2009.

[6] H. Polinder, F. F. A. van der Pijl, G.-J. de Vilder, and P. J. Tavner, "Comparison of direct-drive and geared generator concepts for wind turbines," *IEEE Trans. Energy Convers.*, vol. 21, no. 3, pp. 725–733, Sep. 2006.

[7] V. Yaramasu, B. Wu, P. C. Sen, S. Kouro, and M. Narimani, "High-power wind energy conversion systems: State-of-the-art and emerging technologies," *Proc. IEEE*, vol. 103, no. 5, pp. 740–788.

[8] M. Cheng, P. Han, G. Buja, and G. M. Jovanovi´c, "Emerging multiport electrical machines and systems: Past developments, current challenges and future prospects," *IEEE Trans. Ind. Electron.*, vol. 65, no. 7, pp. 5422–5435, Jul. 2018.

[9] P. Han, M. Cheng, S. Ademi, and M. G. Jovanovic, "Brushless doubly-fed machines: Opportunities and challenges," *Chin. J. Elect. Eng.*, vol. 4, no. 2, pp. 1–17, Jun. 2018.

[10] K. Protsenko and D. Xu, "Modeling and control of brushless doubly-fed induction generators in wind energy applications," *IEEE Trans. Power Electron.*, vol. 23, no. 3, pp. 1191–1197.

[11] S. Shao, E. Abdi, and R. McMahon, "Low-cost variable speed drive based on a brushless doubly-fed motor and a fractional unidirectional converter," *IEEE Trans. Ind. Electron.*, vol. 59, no. 1, pp. 317–325, Jan. 2012.

[12] E. Abdi, M. R. Tatlow, R. A. McMahon, and P. J. Tavner, "Design and performance analysis of a 6 MW medium-speed brushless DFIG," in *Proc. 2nd IET Power Gener. Conf.*, 2013, pp. 1–4.

[13] Y. Liao, L. Xu, and L. Zhen, "Design of a doubly fed reluctance motor for adjustable-speed drives," *IEEE Trans. Ind. Appl* ., vol. 32, no. 5, pp. 1195–1203, Sep./Oct. 1996.

[14] P. Han, J. Zhang, and M. Cheng, "Analytical analysis and performance characterization of brushless doubly-fed machines with multi-barrier rotors," *IEEE Trans. Ind. Appl.*, vol. 55, no. 6, pp. 5758–5767, Nov./Dec. 2019.

[15] M. Cheng, P. Han, and W. Hua, "General airgap field modulation theory for electrical machines," *IEEE Trans. Ind. Electron.*, vol. 64, no. 8, pp. 6063–6074, Aug. 2017.

[16] P. Han, M. Cheng, X. Wei, and N. Li, "Modeling and performance analysis of a dual-stator brushless doubly fed induction machine based on spiral vector theory," *IEEE Trans. Ind. Appl.*, vol. 52, no. 2, pp. 1380–1389, Mar./Apr. 2016.

[17] P. Han, M. Cheng, and R. Luo, "Design and analysis of a brushless doubly-fed induction machine with dual-stator structure," *IEEE Trans. Energy Convers.*, vol. 31, no. 3, pp. 1132–1141, Sep. 2016.

[18] F. Bu, H. Liu, W. Huang, H. Xu, and Y. Hu, "Recent advances and developments in dual stator-winding induction generator and system," *IEEE Trans. Energy Convers.*, vol. 33, no. 3, pp. 1431–1442, Sep. 2018.

[19] R. Li, A. Wallace, Y. Wang, and R. Spee, "Two-axis model development of cage-rotor brushless doubly-fed machines," *IEEE Trans. Energy Convers.*, vol. 6, no. 3, pp. 453–460, Sep. 1991.

[20] F. Barati, S. Shao, E. Abdi, H. Oraee, and R. McMahon, "Generalized vector model for the brushless doubly-fed machine with a nested-loop rotor," *IEEE Trans. Ind. Electron.*, vol. 58, no. 6, pp. 2313–2321, Jun. 2011.

[21] D. Zhou, R. Spee, and G. C. Alexander, "Experimental evaluation of a rotor flux oriented control algorithm for brushless doubly-fed machines," *IEEE Trans. Power Electron.*, vol. 12, no. 1, pp. 72–78, Jan. 1997.

[22] J. Poza, E. Oyarbide, I. Sarasola, and M. Rodriguez, "Vector control design and experimental evaluation for the brushless doubly fed machine," *IET Electr. Power Appl.*, vol. 3, no. 4, pp. 247–256, Jul. 2009.

[23] S. Shao, E. Abdi, F. Barati, and R. McMahon, "Stator-flux-oriented vector control for brushless doubly fed induction generator," *IEEE Trans. Ind. Electron.*, vol. 56, no. 10, pp. 4220–4228, Oct. 2009.

[24] J. Hu, J. Zhu, and D. G. Dorrell, "A new control method of cascaded brushless doubly fed induction generators using direct power control," *IEEE Trans. Energy Convers.*, vol. 29, no. 3, pp. 771–779, Sep. 2014.

[25] R. Sadeghi, S. M. Madani, and M. Ataei, "A new smooth synchronization of brushless doubly-fed induction generator by applying a proposed machine model," *IEEE Trans. Sustain. Energy*, vol. 9, no. 1, pp. 371–380, Jan. 2018.

[26] X. Wei, M. Cheng, J. Zhu, H. Yang, and R. Luo, "Finite-set model predictive power control of brushless doubly fed twin stator induction generator," *IEEE Trans. Power Electron.*, vol. 34, no. 3, pp. 2300–2311, Mar. 2019.

[27] D. Zhu, X. Zou, S. Zhou, W. Dong, Y. Kang, and J. Hu, "Feedforward current references control for DFIG-based wind turbine to improve transient control performance during grid faults," *IEEE Trans. Energy Convers.*, vol. 33, no. 2, pp. 670–681, Jun. 2018.

[28] Y. Zhou, P. Bauer, J. A. Ferreira, and J. Pierik, "Operation of grid-connected DFIG under unbalanced grid voltage condition," *IEEE Trans. Energy Convers.*, vol. 24, no. 1, pp. 240–246, Mar. 2009.

[29] J. Hu, H. Xu, and Y. He, "Coordinated control of DFIG's RSC and GSC under generalized unbalanced and distorted grid voltage conditions," *IEEE Trans. Ind. Electron.*, vol. 60, no. 7, pp. 2808–2819, Jul. 2013.

[30] J. Hu, H. Nian, H. Xu, and Y. He, "Dynamic modeling and improved control of DFIG under distorted grid voltage conditions," *IEEE Trans. Energy Convers.*, vol. 26, no. 1, pp. 163–175, Mar. 2011.

[31] H. Nian and Y. Song, "Direct power control of doubly fed induction generator under distorted grid voltage," *IEEE Trans. Power Electron.*, vol. 29, no. 2, pp. 894–905, Feb. 2014.
[32] S. Shao, T. Long, E. Abdi, and R. A. McMahon, "Dynamic control of the brushless doubly fed induction generator under unbalanced operation," *IEEE Trans. Ind. Electron.*, vol. 60, no. 6, pp. 2465–2476, Jun. 2013.
[33] J. Chen, W. Zhang, B. Chen, and Y. Ma, "Improved vector control of brushless doubly fed induction generator under unbalanced grid conditions for offshore wind power generation," *IEEE Trans. Energy Convers.*, vol. 31, no. 1, pp. 293–302, Mar. 2016.
[34] G. Dauksha and G. Iwanski, "Indirect torque control of a cascaded brushless doubly-fed induction generator operating with unbalanced power grid," *IEEE Trans. Energy Convers.*, vol. 35, no. 2, pp. 1065–1077, Jun. 2020.
[35] A. Petersson, L. Harnefors, and T. Thiringer, "Evaluation of current control methods for wind turbines using doubly-fed induction machines," *IEEE Trans. Power Electron.*, vol. 20, no. 1, pp. 227–235, Jan. 2005.
[36] M. Cheng, R. Luo, and X. Wei, "Design and analysis of current control methods for brushless doubly fed induction machines," *IEEE Trans. Ind. Electron.*, vol. 66, no. 1, pp. 717–727, Jan. 2019.
[37] P. Rodriguez, A. Luna, I. Candela, R. Mujal, R. Teodorescu, and F. Blaabjerg, "Multiresonant frequency-locked loop for grid synchronization of power converters under distorted grid conditions," *IEEE Trans. Ind. Electron.*, vol. 58, no. 1, pp. 127–138, Jan. 2011.

Litong Xu (Student Member, IEEE) received the B.Sc. degree in electrical engineering in 2018 from the School of Electrical Engineering, Southeast University, Nanjing, China, where he is currently working toward the M.Sc. degree.

His current research interests mainly include the analysis and control of brushless doubly fed induction machines in wind energy conversion systems.

Ming Cheng (Fellow, IEEE) received the B.Sc. and M.Sc. degrees from Southeast University, Nanjing, China, in 1982 and 1987, respectively, and the Ph.D. degree from The University of Hong Kong, Hong Kong, in 2001, all in electrical engineering.

Since 1987, he has been with Southeast University, Nanjing, where he is currently a Chief Professor with the School of Electrical Engineering and the Director of the Research Center for Wind Power Generation. From January to April 2011, he was a Visiting Professor with the Wisconsin Electric Machine and Power Electronics Consortium, University of Wisconsin–Madison, Madison, WI, USA. His teaching and research interests include electrical machines, motor drives for electric vehicles, and renewable energy generation. He is the author or co-author of more than 400 technical papers and six books, and is the holder of 130 patents in his areas of interest.

Dr. Cheng is a Fellow of the Institution of Engineering and Technology, U.K. He was a Distinguished Lecturer of the IEEE Industry Applications Society from 2015 to 2016.

He has served as the Chair and an Organizing Committee Member for numerous international conferences.

Xinchi Wei (Member, IEEE) received the Ph.D. degree in electrical engineering from Southeast University, Nanjing, China, in 2018.

From June 2016 to June 2017, she was a Joint Ph.D. Student funded by China Scholarship Council with the School of Electrical, Mechanical and Mechatronic Systems, University of Technology Sydney, Ultimo NSW, Australia. Since 2018, she has been with State Grid Shanghai Electric Power Research Institute, Shanghai, China. Her research interests include renewable energy systems, smart grids, electrical machines, and power electronics.

Xiaoming Yan (Student Member, IEEE) received the M.Eng. degree in control engineering from Northeastern University, Shenyang, China, in 2018. He is currently working toward the Ph.D. degree in electrical engineering with Southeast University, Nanjing, China.

His research interests include the control of brushless doubly fed induction machines for wind power systems.

Yu Zeng (Student Member, IEEE) received the B.Sc. and M.Sc. degrees in electrical engineering from Jiangsu University, Zhenjiang, China, in 2014 and 2017, respectively. He is currently working toward the Ph.D. degree in electrical engineering with Southeast University, Nanjing, China.

His research interests include the design and analysis of permanent magnet synchronous machines and brushless doubly fed machines.